Silicon (2022) 14:2545–2553
https://doi.org/10.1007/s12633-021-01037-z

ORIGINAL PAPER

[Ni-Mo-Si]:Nb Bulk Metallic Glasses: Microstructure, Mechanical and Corrosion Studies

Gayatri Tanuja Guddla[1] · Satyadevi Ambadipudi[1] · Shanti Yenduva[1] · Vamsi Krishna Katta[2] · Balaji Rao Ravuri[2]

Received: 1 January 2021 / Accepted: 25 February 2021 / Published online: 11 March 2021

Abstract

We examine the effect of substituting Niobium (Nb), on the glass-forming abilities (GFA), mechanical and corrosion properties of bulk metallic glasses (BMGs). BMGs are synthesized using the general formula of $(Ni_{75}Mo_{15}Si_{10})_{100-x}Nb_x$ (x = 0, 5, 10 and 15 at.%, labeled as $NMSNb_0$, $NMSNb_5$, $NMSNb_{10}$ and $NMSNb_{15}$) that are synthesized using high energy mechanical ball milling technique. Thermal, mechanical, and corrosion properties were enhanced significantly with an increase in Niobium (Nb) content of 10 at.% ($NMSNb_{10}$). Using XRD analysis, the analysis related to phase attribution and crystallizability is scrutinized. Alloying this BMG with Molybdenum (Mo) and Niobium (Nb) helped avoid embrittlement in the sulphuric acid environment, overcoming strain cracking problems caused during welding, preventing pitting, crevice corrosion, and wet corrosion. Applicability of the present BMG system is examined in light of the correlation between morphology, mechanical, and corrosion studies.

Keywords Glass-forming ability · Bulk metallic glass · Mechanical properties

1 Introduction

Among the variety of glass-based material systems, bulk metallic glasses (BMGs) are the modern classical engineering material systems in this decade [1–3]. The structural and excellent functional characteristics (high strength, thermal, mechanical, and anti-corrosion) of BMGs, create a lot of interest to meet the technological significance in the modern industry [1–3]. However, BMGs exhibit relatively brittle, low mechanical, ductility, and corrosive properties at high temperature due to their limited thermal stability against crystallization, preventing them from being commercialized [4, 5]. More recently, the publication rate is being increased vertically to search for new multi-component BMG systems based on tri-component rule validity [6]. Also, achieving ultra-high-strength and thermal stability due to atoms' random arrangement without long-range order in the structure can significantly enhance their mechanical and corrosion properties [6–8]. For instance, Aytekin Hitit et al. demonstrated Ni-based BGMs with high thermal stability and hardness over high corrosion resistance and the ability to be electroplated with other metals as protective coatings [9]. The corrosion resistance and nickel alloy strength can be highly enhanced by alloying with Molybdenum (Mo) metal [10]. Silicon (Si) is a primary fundamental element, demonstrating its essential role in the glass formation of BMGs. Liang WZ et al. reported the effect of Si addition on the glass-forming ability (GFA), which exhibits a uniform plastic deformation and a considerable plastic strain [11]. The advantages of doping with Niobium (Nb) in BMGs include: (i) improving the GFA; (ii) enhancing the properties including thermal stability, mechanical, physicochemical properties of the BMGs [12]. Nevertheless, it is well understood that minor alloying can significantly affect the performance of BMGs. Inspired by all these significant knowledge findings, we have examined in this article, the glass-forming abilities, mechanical and corrosion properties of the ternary alloy [Ni-Mo-Si], doped with Niobium (Nb) at the concentrations, Nb_x (x = 0, 5, 10 and 15 at.%) characterized by XRD, DTA, Vickers Hardness test, Polarization test and then SEM before and after corrosion test. This investigation shows that even 0.1 % Niobium (Nb) can significantly

✉ Balaji Rao Ravuri
ravuri3091@yahoo.co.in

[1] Department of Mechanical Engineering, School of Technology, GITAM (Deemed to be University), Hyderabad 502329, India

[2] Department of Physics, School of Science, GITAM (Deemed to be University), 502329 Hyderabad, India

enhance performance and offer excellent oxidation and corrosion resistance. A variety of synthesis methods have been adopted: magnetron sputtering, melt spinning, pulsed laser spinning, high energy ball milling, etc. [13–15]. Among them, a high energy ball milling technique is regarded as a flexible and straightforward technique. The same approach is employed in this investigation to synthesize $[Ni\text{-}Mo\text{-}Si]_{100-x}$:$Nb_x$ BMG glass systems due to the following advantages; (i) during the process of milling, microstructure determines plastic deformation which will help to determine fracture morphology and particle welding systematically, (ii) milling process generates stress in the powder mixture which controls the degree of crystallization to a required degree [16, 17].

2 Experimental

Ni-Mo-Si pure metal powders with high purity, Nickel (Ni, 99.99 at.%), Molybdenum (Mo, 99.99 at.%) and Silicon (Si, 99.99 at.%) and Niobium (Nb, 99.99 at.%) were mixed well with a formula $(Ni_{75}Mo_{15}Si_{10})_{100-x}Nb_x$ (x = 0 to 15 at.%, labelled as $NMSNb_x$) for about 30 min to form a homogenous mixture. These metal compositions are mixed further and crushed to micro and even nano-size, using a high energy ball milling apparatus, using a tungsten carbide crucible, with powder to balls ratio taken as 1:10, for about 30 h with a speed of 300 rpm. The vials are evacuated and purged with Ar gas at a pressure of 3×10^5 Pa, initially. Owing to control agglomeration of particles, milling is carried in a wet medium by adding 30 ml of hexane. Vials are generally be opened inside the glove box and cleaned every time to manage the powder mixture's uniform homogeneity; however, a little contamination is observed. ICP Spectroscopy is used to analyze the as-prepared powder mixture where the iron and oxygen contents approximately 0.4 and 1.0 mol%, respectively. This sample's amorphous nature was investigated by XRD analysis, before and after ball milling by X-ray powder diffraction (XRD) using PANalytical diffractometer (Cu-Kα radiation) at a scanning step of 0.01° in the 2θ range.

The thermal properties are characterized using a DTA (Differential Thermal Analysis) under Ar atmosphere with a 10 K/min heating rate. The prepared BMG milled powders are then pressed with a pressure of 1.2 GPa using a vacuum hot-pressing machine between T_g and T_c for about an hour to attain green pellets. The samples are then made into 10mm x 2mm pellets using an automatic pelletizer. Hardness tests were done using Vickers indenter (Wolpert Wilson, Universal 930/250 N DigiTestor) with 10 s dwell time at a load of 1 kg. 3369 Uniaxial Compression Testing machine is used to perform the compression tests at a loading rate of 2×10^{-4}/s and an aspect ratio of 2:1.

The crystallite sizes were studied using SIRION SEM (Scanning Electron Microscopy) apparatus at 20 kV before and after the corrosion test. An electron microscope is used to analyze the TEM-scanned images and study all the samples (Jeol JEM-1010). The samples to be tested are maintained dry and electrically conductive. The prepared samples' corrosive nature was investigated using electrochemical polarization technique with RST500F device in HCL aqueous solution from − 2.5 V ~ 5.5 V at a potential sweep rate of 0.05 mV/s. This test is done with a standard SCE (Saturated Calomel Electrode) as a reference electrode. A three-electrode cell, along with a platinum foil, is taken as a counter electrode.

3 Results

During the milling process, the energy absorbed by the metal powder mixture will be utilized to monitor its crystalline ratio to an amorphous phase as a function of milling time. Subsequently, phase details, size of unprocessed crystallites and strain attained by a lattice can be obtained. The XRD profiles of all synthesized, $(Ni_{75}Mo_{15}Si_{10})_{100-x}Nb_x$ BMG powder mixtures, before and after ball milling for 2 h, 15 h, and 30 h, respectively, are shown in Fig. 1a, b and c. Rietveld's refinement is applied to analyze the powder full peak pattern matching. The diffraction peaks corresponding to Nickel (Ni), Molybdenum (Mo), Silicon (Si) and Niobium (Nb) crystalline phases (nickel (Ni, ICSD PDF No: 98-005-2852), molybdenum (Mo, ICSD PDF No: 98-005-2852), silicon (Si, ICSD PDF No: 98-005-2852) and niobium (Nb, ICSD PDF No: 98-005-2852)) can be observed in the XRD peak profiles for 2 h of milling time (Fig. 1).

From 2 h to 15 h, it is noteworthy to understand that Ni, Mo, and Si's peak intensities are gradually decreasing and can be seen slightly at 15 h of milling time. Whereas the peak intensity of 'Nb' appeared to be more and more broaden at 2θ = 37° to 43°. This is evidence of grain growth refinement mechanism, occurred in BMGs against milling time. Additionally, the grain growth refinement is gradually shaped into a complete amorphous phase along with the co-existence of 'Nb' nanocrystallites unprocessed up to 30 h of milling time. These unprocessed 'Nb' crystallites promote nanocrystallization in the present $(Ni_{75}Mo_{15}Si_{10})_{100-x}Nb_x$ BMG system, resulting in precipitated nanocrystalline phases. As precipitated, nanocrystalline phases will activate the blending of powder mixture to a greater extent to meet the perfect chemical homogeneity.

Nevertheless, TEM images are recorded for all the $NMSNb_x$ samples for 30 h milling time, and among all, Nb_{10} sample displays a clear presence of 'Nb' crystallites coupled with perfect amorphous nature. Further, there is no appreciable modification in the morphology, even up to 80 h, which confirms that 30 h of milling time is adequate to achieve best supercooled region of BMGs. To justify this, we have recorded the TEM image and its SAED pattern for

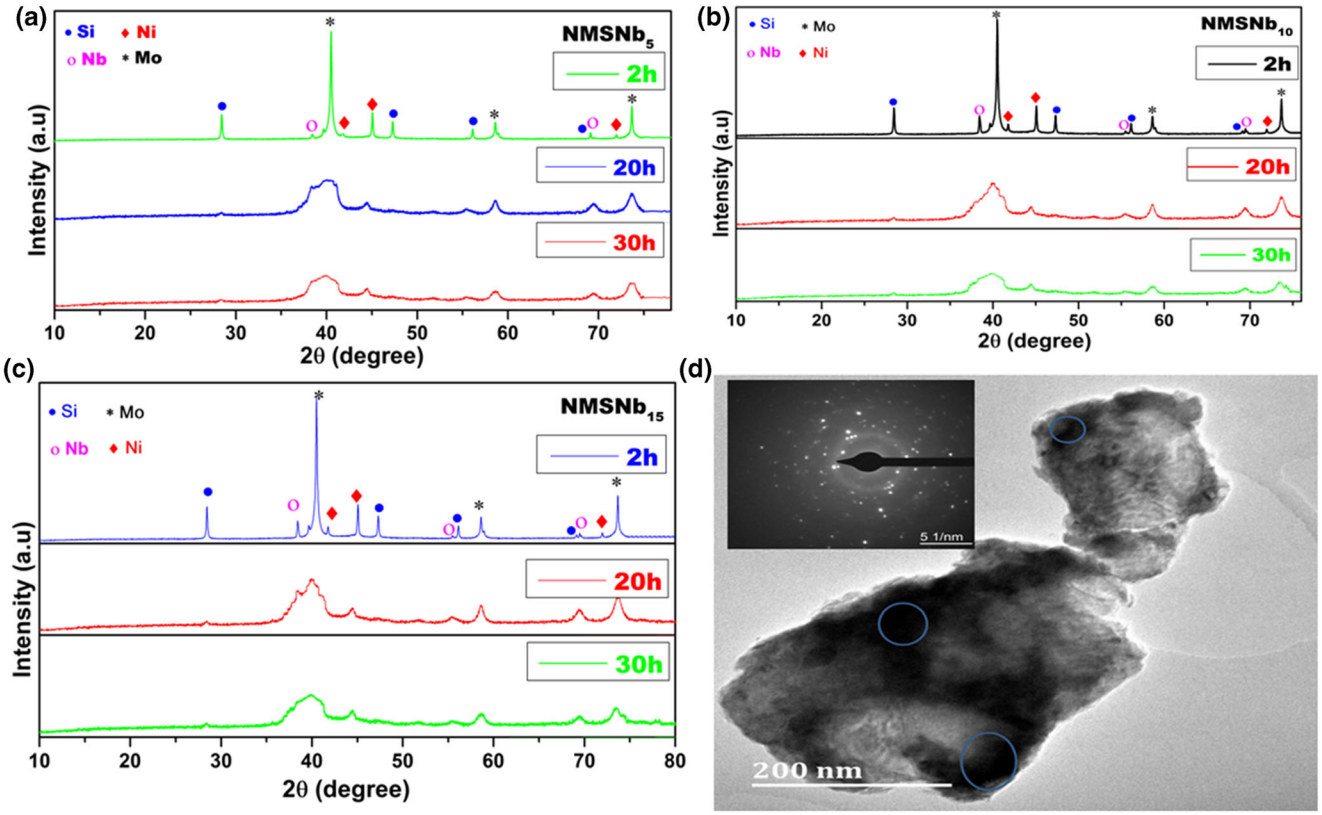

Fig. 1 XRD traces of all the as-prepared Nb_x (x = 5, 10, and 15 at.%) BMG powder mixture for milling times 2 h, 20 h and 30 h. **d** TEM bright-field image for 30 h of milling time for $NMSNb_{10}$ BMG sample

the Nb_{10} sample at 30 h of milling time (Fig. 1d). Where precipitation of crystalline phases around amorphous background can be seen, resulting in its chemical homogeneity (Fig. 1d). Eventually, it is also essential to explain why XRD traces are seemed to be irregular, which reveals that the present BMG powder mixture is oxidized partially (Fig. 1a, b and c). Hence, it again proved that the high-energy ball milling method is an adequate one to prepare $(Ni_{75}Mo_{15}Si_{10})_{100-x}Nb_x$ BMG within the limit of composition [18, 19]. The crystallite size and lattice strain of all Nb_x samples can be calculated from peak broadening of XRD using the Scherer formula (Eq. 1) and Williamson–Hall analysis (Eq. 2).

$$D = \frac{0.94\lambda}{\beta \cos\theta} \tag{1}$$

$$\beta \cos\theta = \frac{0.94\lambda}{D} + 4\varepsilon \sin\theta \tag{2}$$

Where β is FWHM (Full-Width Half Maximum) value, θ is Bragg angle, D is the size of the crystallites (nm), ε is lattice strain, and λ is the wavelength (0.1540562 nm) of X-ray, respectively. The average size of the crystallites varies from 35 nm to 50 nm as a function of x. These values are appropriate in size due to perfect mechanical deformation for 30 h of milling time [20] (Table 1).

Now, FE-SEM images are utilized to monitor all the Nb_x BMG samples' morphology for 30 h milling time (Fig. 2). Here, the presence of 'Nb' nanoparticles with size ranges from 35 nm to 50 nm can be seen against an amorphous background, which is directly related to hot consolidation of powder mixture [21]. It is also evident that this hot consolidation technique is an effective one to make of dense BMG network. Hence, it is again proved that hot consolidation process is a successful one to make dense BMG network [21]. Therefore, it is well understood that the process of milling migrates the fresh powder mixtures into a BMG network due to cold welding and further variation of powder particles from micro

Table 1 Crystallite size and lattice strain of all $NMSNb_x$ (x = 0, 5, 10 and 15 at.%) BMG samples for 30 h of milling time

BMG	Crystallite size (nm)	Lattice strain (%)
$NMSNb_0$	60	1.5
$NMSNb_5$	40	1.5
$NMSNb_{10}$	35	0.9
$NMSNb_{15}$	42	1.2

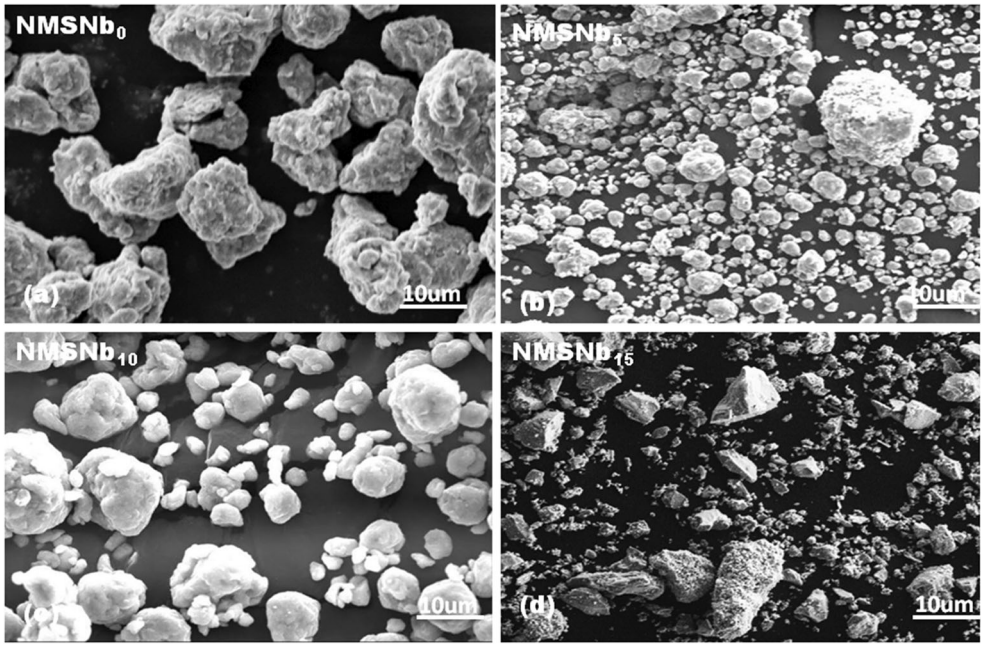

Fig. 2 FE-SEM images for all the Nb_x (x = 5, 10 and 15 at.%) BMG networks for 30 h of milling time

to nano. Eventually, it can be noted down that the energy supplied to the powder mixture during the process of milling favors converting an ordered intermetallic structure to an amorphous glass structure as justified in XRD result analysis.

To further investigate the amorphous nature of the prepared samples of BMGs for 30 h of milling time, DTA tests were done at a heating rate of 10 K/min, shown in Fig. 3.

The exothermic and endothermic tendency profiles can be seen clearly to make a note of glass transition and super cooled regions [22]. DTA parameters such as (T_g, (glass transition temperature), (T_c (crystallization temperature)), (T_l (liquidus temperature)), ($\Delta T = T_c - T_g$, (super-cooled liquid region)), ($T_{rg}=T_l/T_g$, (reduced glass transition temperature)), and also ($\gamma = T_c/(T_g+T_l)$, (parameter)) are obtained via profiles for all $NMSNb_x$ BMG samples and listed in Table 2 [6, 16]. From Table 2, it is noteworthy to mention that the values of super-cooled liquid region and the parameter γ are decreased from $NMSNb_{10}$ to $NMSNb_0$ [23, 24]. Figure 4 is presented to examine the relationship between ΔT and the parameter γ as a function of Nb content in the BMG powder mixture which indicates that the $NMSNb_{10}$ sample is observed to achieve best glass-forming ability (ΔT) and γ parameter and is directly supported by the value of T_{rg} ($T_{rg} > 0.5$) [25]. According to Turnbull, the value of T_{rg} is higher than 0.5; better will be the thermal stability and glass-forming ability, which is a significant factor of this family of $(Ni_{75}Mo_{15}Si_{10})_{100-x}Nb_x$ BMG network as T_{rg} values for all the $NMSNb_x$ sample are higher than 0.5 [25].

The Vickers Hardness test results can be seen from Fig. 4, for all the $NMSNb_x$ BMG samples. It can be concluded from Figs. 3 and 4 that the $NMSNb_{10}$ sample relatively exhibits the highest glass-forming ability and highest hardness property. This can be attributed to the large negative heating effect produced upon quantitative substitution of niobium (Nb_x) over the base $(Ni_{75}Mo_{15}Si_{10})_{100-x}$ BMG network, which favours

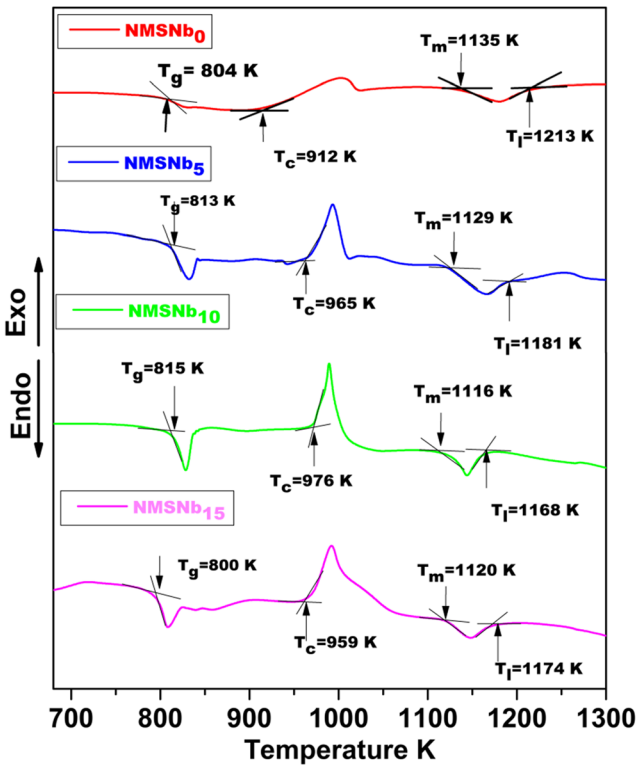

Fig. 3 DTA profiles all as prepared $NMSNb_x$ BMG samples at 30 h of ball milling

Table 2 DTA parameters of all as prepared $NMSNb_x$ BMG samples after 30 h of ball milling

BMG	T_g (K)	T_c (K)	T_m (K)	T_l (K)	$\Delta T=T_c-T_g$ (K)	$\gamma=T_c/(T_g+T_l)$	$T_{rg}=T_g/T_l$
$NMSNb_0$	804	912	1135	1213	108	0.452	0.662
$NMSNb_5$	813	965	1129	1181	152	0.483	0.688
$NMSNb_{10}$	815	976	1116	1168	161	0.492	0.677
$NMSNb_{15}$	800	959	1120	1174	159	0.485	0.681

obtaining an appreciable change in hardness during hardness test. The prepared samples' mechanical behavior of all $NMSNb_x$ samples exhibit a unique behavior of increasing stress with the increase of strain, which is also called work hardening [1, 18–21]. Compressive stress-strain curves for all the $NMSNb_x$ BMG samples for 30 h of milling are shown in Fig. 5.

All these curves undergo elastic deformation and then a serrated plastic deformation before the fracture failure; however, a specific yielding point connected to a definite strain value can be shown (Fig. 5) [20]. The yield strength (σ_y) and fracture strength (σ_f) values are obtained to be minimum, whereas plastic strain (ε_p) and hardness are achieved to be maximum for $NMSNb_{10}$ sample (Table 3). The substitution of optimal quantities of Nb content (10 at.%) in the $Ni_{75}Mo_{15}Si_{10}$ BMG network triggers a positive heating effect, resulting in the irregularity in the atomic size variations during the blending of constituent elements in the present BMG network. This tendency will create a heterogeneous environment for the entire region of the amorphous part of the BMG network, resulting in observing the sites related to shear bands' presence and thin potential barriers. The compositional dependence of plastic strain (ε_p) and hardness reveals that $NMSNb_{10}$ BMG sample is achieved to be maximum, which might be due to the formation of an adequate number of shear bands across the amorphous region (Fig. 6).

However, as the 'Nb' content increases beyond 10 at.%, the repulsion between the intermetallics is activated due to the aggregation of 'Nb' particles resulting from minimizing the plastic strain (ε_p) and hardness (Fig. 7), which is a prominent characteristic feature of this $(Ni_{75}Mo_{15}Si_{10})_{100-x}$ Nb_x family of BMG network. Nevertheless, it is also equally important to analyze the surface morphology of all $NMSNb_x$ BMG at 30 h of milling time samples after compression test via FE-SEM images (Fig. 8a-d). Herein, BMG network is critically precipitated with 'Nb' nanoparticles, leading to crystallization around the amorphous background of BMG system (Fig. 8). Also, the clustering region gradually diminished as 'Nb' content increases from 2 at.% and almost disappeared for 10 at.% of 'Nb' content (Fig. 8c). Figure 8d is depicted that excessive agglomeration can be viewed clearly because of uncontrolled aggregation of single 'Nb' nanoparticles beyond 10 at.% of 'Nb' content, which hampers the corrosion resistance. This behavior can be viewed very clearly from SEM image of

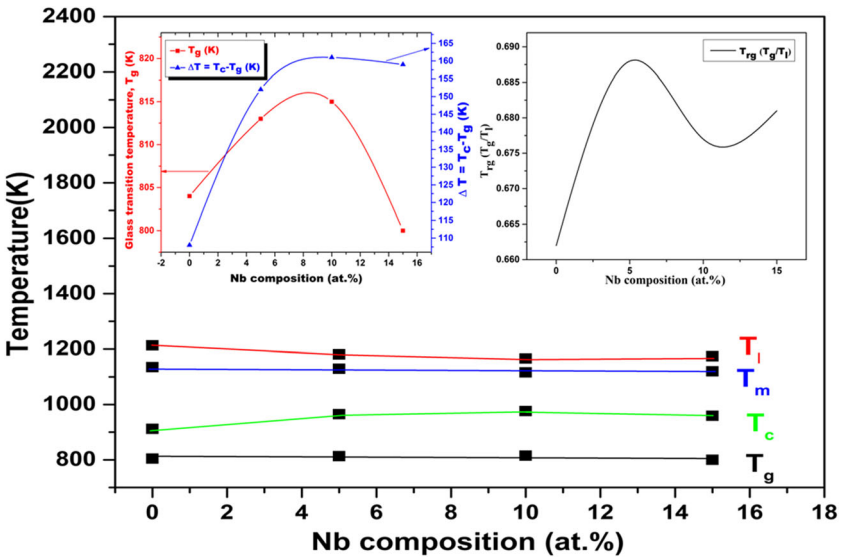

Fig. 4 Compositional dependence of differential thermal parameters (T_g, T_c, T_m, T_l, ΔT, γ, and T_{rg})

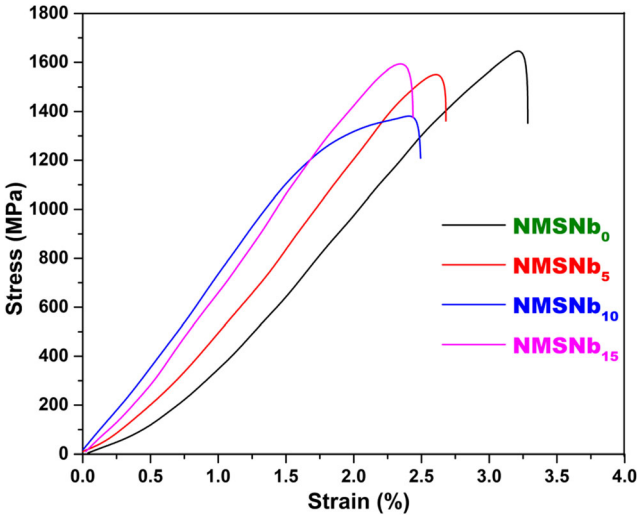

Fig. 5 Stress-strain curves of all as prepared $NMSNb_x$ BMG samples

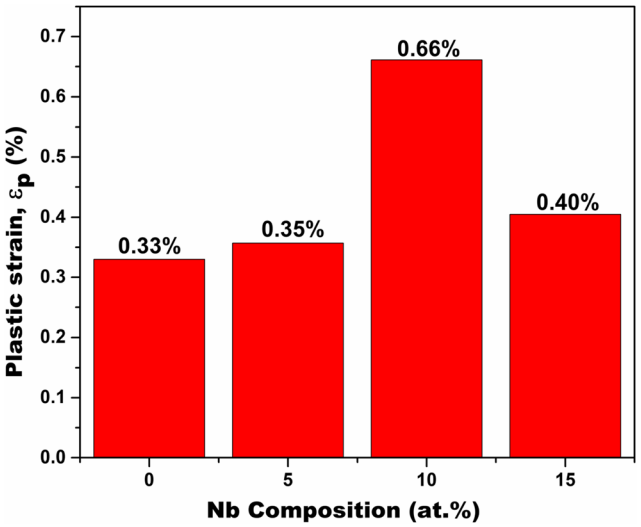

Fig. 6 Compressive plasticity of all as prepared $NMSNb_x$ BMG samples

$NMSNb_{10}$ sample (Fig. 8c) where microstructural morphology is appeared to have coexisted with the best plastic and corrosive resistant relative to other samples.

To examine the corrosion tendency against 'Nb' concentration, potentiodynamic polarization tests are employed by mixing the 0.5 M HCl with an applied voltage and sweep rate in the order of -2.5V ~ 5.5V and 0.05mV/s respectively. Subsequently, polarization curves related to electrodes profile for all Nb_x BMG samples, as depicted in Fig. 9a and b. It is to be noted from Fig. 9a and b that all these polarization curves follow a uniform tendency. It is essential to know that all these anode curves could not follow the path (active and passive transition) of 'Tafel' curve since each curve's slope extends flipside to the corrosion potential [26]. Nevertheless, the polarisation curve of $NMSNb_{10}$ displays superior step height and serration fluctuation relatively than other compositions under investigation, which stands as an applicable property of the present BMG system for potential applications. Furthermore, potentiometric parameters such as electrode current densities (both cathode (i_c) and anode (i_p)) with which total positive current density be obtained by summing them together (Fig. 9b). The summary of all the potentiometric parameters is listed in Table 4.

Table 3 Yield strength (σ_y), fracture strength (σ_f), and plastic strain (ε_p) of all as prepared $NMSNb_x$ BMG samples

BMG	σ_y (MPa)	σ_f (MPa)	ε_p (%)	Hardness (HV)
$NMSNb_0$	1701±22	1732±36	0.33±0.1	573
$NMSNb_5$	1412±33	1557±32	0.357±0.1	428
$NMSNb_{10}$	1262±21	1378±12	0.661±0.1	575
$NMSNb_{15}$	1396±17	1598±23	0.405±0.1	497

It is observed from Table 4 that the passive current density (i_p) increases from $NMSNb_0$ to $NMSNb_{10}$ and becomes almost plateau, can be stated as the corrosion tendency of the present BMG system (Table 4). The variation of 'E_c' (corrosion potential) and i_c (corrosion current density) with 'Nb' content can be presented in Fig. 10a. The inverse correlation reveals that a sample delivering the lowest current density (i_c), gains the highest corrosion potential (E_c) (Fig. 10a). Whereas both passive current (i_p) and potential (E_p) exhibit similar behavior and show minimum value for 10 at.% of Nb content ($NMSNb_{10}$). As a result, all this data related to potentiometric parameters (i_c, E_c and i_p, E_p) reveals that the active sample $NMSNb_{10}$ achieved to be highest resistivity towards corrosion and self-passivization tendency which barely forms passive film than other sample of present $(Ni_{75}Mo_{15}Si_{10})_{100-x}$ Nb_x family of BMG network (Fig. 10b) (Table 4) [27, 28].

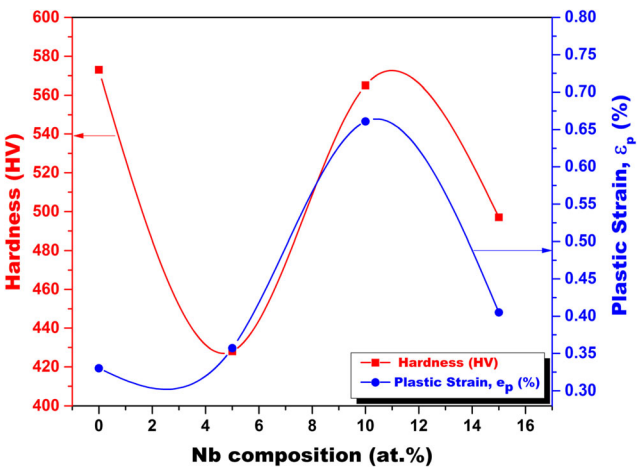

Fig. 7 Correlation between Vickers hardness and plastic strain values of all as prepared $NMSNb_x$ BMG samples

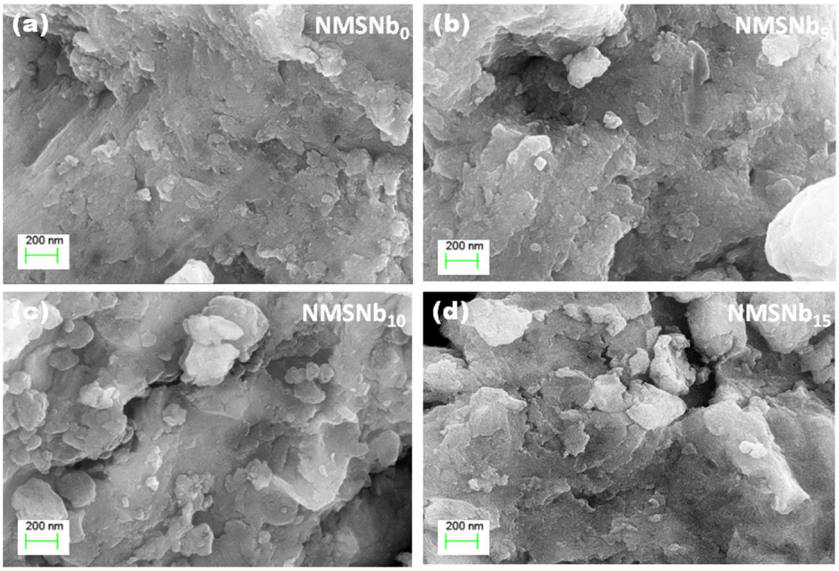

Fig. 8 **a-d** SEM images of all as prepared $NMSNb_x$ BMG samples at 30 h ball milling before corrosion tests

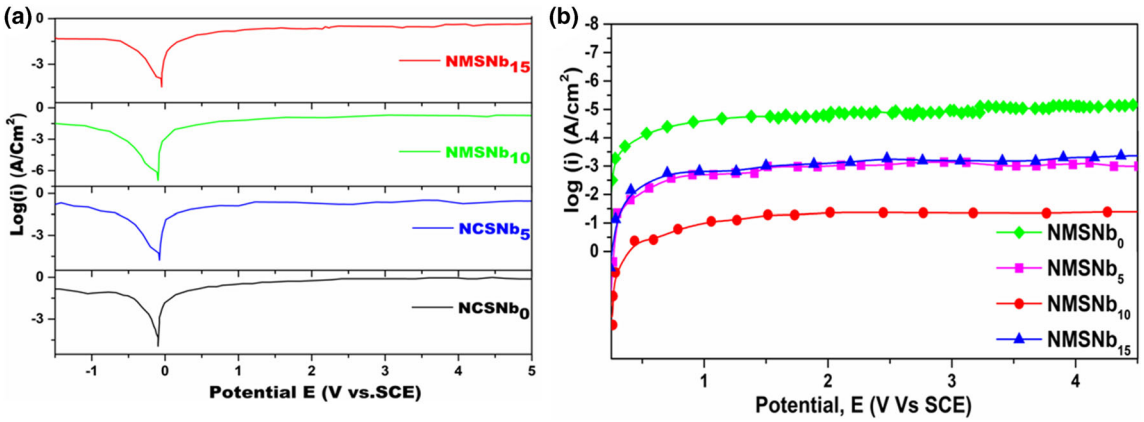

Fig. 9 (**a**) Potentiometric analysis of $NMSNb_x$ BMG samples at 30 h of ball milling - Anodic current density with corrosion potential (**b**) Potentio-metric analysis of $NMSNb_x$ BMG samples with 8 mm diameter- Magnification images of (**a**)

It is mandatory to examine the corrosion resistivity retention even after the polarization test; we have recorded the FE-SEM images, as shown in Fig. 11a-d. Figure 11a shows that the surface morphology appears with an exact amorphous phase as there is no 'Nb' content in the BMG system ($NMSNb_0$ sample). However, gradual increment in the degree of crystallization due to the crystalizable capability of 'Nb' nano-crystalllites base $(Ni_{75}Mo_{15}Si_{10})_{100-x}$ BMG network. Moreover, the presence of an oxide layer is also witnessed by unidentified agglomeration on every surface, clearly stated in the XRD analysis of the earlier section (Fig. 11a-d) [29]. Among all the samples of $(Ni_{75}Mo_{15}Si_{10})_{100-x}Nb_x$ BMG system under investigation, $NMSNb_{10}$ sample $((Ni_{75}Mo_{15}Si_{10})_{90}Nb_{10})$ exhibits superior corrosion resistance and low current density, which confirms as a

Table 4 Corrosion potential (E_c), passive potential (E_p), corrosion current density (i_c), passive current density (i_p) of all as prepared $NMSNb_x$ BMG samples

BMG	E_c (mV)	E_p (V)	i_c (A/cm^2)	i_p (A/cm^2)
$NMSNb_0$	-109.21	1.331	4.6×10^{-2}	0.5687
$NMSNb_5$	-80.46	0.72	2.1×10^{-2}	0.41
$NMSNb_{10}$	-61.2	0.51	4.1×10^{-4}	0.0066
$NMSNb_{15}$	-85.6	0.89	3.2×10^{-2}	0.51

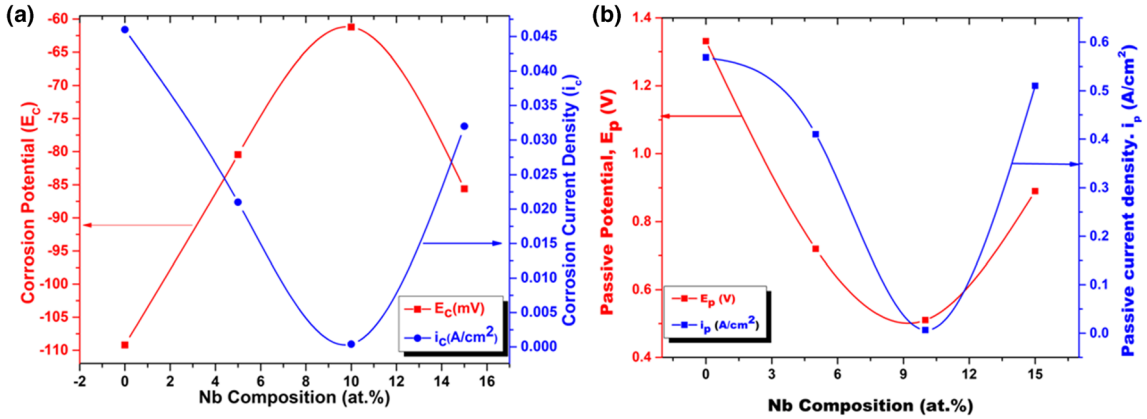

Fig. 10 (**a**) Compositional dependence between corrosion current density (i_c) and corrosion potential (E_c) Values (**b**) Compositional dependence between passive current density (i_p) and passive potential (E_p) Values

potential candidate for use in lightweight transportation applications relative to others.

4 Conclusions

i) XRD analysis pointed out that the unprocessed 'Nb' crystallites even for 30 h of milling time promotes the process of nanocrystallization to precipitate nanocrystalline phases, which will activate the blending of powder mixture to a greater extent to meet the perfect chemical homogeneity.

ii) Reduced glass transition temperature (T_{rg}) values for all the Nb_x samples are higher than 0.5; confirms their superior thermal stability and glass-forming ability, which is a crucial feature of this family of $(Ni_{75}Mo_{15}Si_{10})_{100-x}$ Nb_x BMG network.

iii) The substitution of optimal quantities of Nb content (10 at.%) in the $(Ni_{75}Mo_{15}Si_{10})_{100-x}$ Nb_x ($NMSNb_{10}$) BMG network triggers a positive heating effect resulting from forming the irregularity in the atomic size variations during the blending of constituent elements.

iv) Potentiometric parameters (i_c, E_c, and i_p, E_p) reveal that the active sample $NMSNb_{10}$ achieved the highest resistivity towards corrosion and self-passivization tendency than all other samples present as evident from SEM images before and after corrosion tests.

Summing the results together, the present $(Ni_{75}Mo_{15}Si_{10})_{100-x}Nb_x$ BMG network is expected to attract special attention for lightweight transportation applications owing to its superior functional characteristics, reduced glass transition temperature (T_{rg}>0.5), hardness, resistivity towards corrosion, and self-passivization tendency.

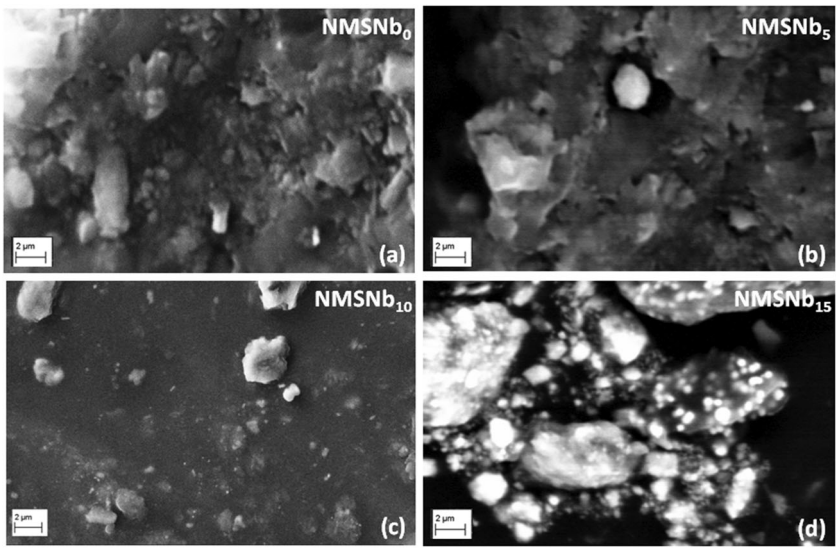

Fig. 11 SEM micrographs of the corroded surfaces of all as prepared $NMSNb_x$ BMG samples

Acknowledgements The author wishes to thank Prof. Jonnalagadda B Srikanth, School of Chemistry and Physics, University of KwaZulu Natal (UKZN), Westville Campus, Durban, South Africa for his kind support to carryout electron microscopy images and analysis.

Author Contributions Gayatri Tanuja Guddla: Experimental work and contributed to the final manuscript.

Satyadevi Ambadipudi: Verified the analytical methods.

Shanti Yenduva: Performed the computations.

Vamsi Krishna Katta: Helped to review the Results and also discussion.

Balaji Rao Ravuri: Conceived of the presented idea and supervised the findings of this work.

Data Availability The data related to the experimental work upon demand.

Declarations

Conflict of Interest The authors have declared that no conflict of interest exists.

Human and Animal Rights This article does not contain any studies with human participants or animals performed by any of the authors.

Consent to Participate Informed consent was obtained from all individual participants included in the study.

Consent for Publication We give our consent for the publication of identifiable details, which can include photograph(s) and/or videos and/or case history and/or details within the text ("Material") to be published in the this Journal.

References

1. Yokoyama Y, Inoue H, Fukaura K, Inoue A (2002) Mater Trans 43: 575–579
2. Wu Y, Wang H, Wu H et al (2011) Acta Mater 59(8):2928–2936
3. Inoue A, Zhang W, Zhang T, Kurosaka K (2002) J Non-Cryst Solids 304:200–209
4. Vincent S, Murty B, Kramer M, Bhatt J (2015) Mater Des (1980–2015) 65:98–103
5. Zhang L-k, Chen Z-h, Zheng Q, Chen D (2013) Matter 411:149–153
6. Inoue A (2001) Mater Sci Eng A 304:1–10
7. Johnson W (2002) Jom 54:40–43
8. Wang D, Li Y, Sun B, Sui M, Lu K, Ma E (2004) Appl Phys Lett 84:4029–4031
9. Hitit A, Şahin H, Öztürk P, Aşgın AM (2015) Metal 5:162–171
10. Zhang X, Ma E, Xu J (2006) J Non-Cryst Solids 352:3985–3994
11. Kim J, Kyeong JS, Ham M-H, Minor AM, Kim DH, Park ES (2016) Mater Des 98:31–40
12. Cao G, Liu K, Liu G, Zong H, Bala H, Zhang B (2019) J Non-Cryst Solids 513:105–110
13. Lin CJ, Spaepen F (1982) Appl Phys Lett 41:721–723
14. Filipecka K, Pawlik P, Filipecki J (2017) J Alloy Comp 694:228–234
15. Liu Y, Padmanabhan J, Cheung B et al (2016) Sci Rep 6:1–8
16. Ramasamy P, Shahid RN, Scudino S, Eckert J, Stoica M (2017) J Non-Cryst Solids 725:227–236
17. Chen C-L, Huang C-L (2014) Int J Refract Hard Met 44:19–26
18. El-Eskandarany MS, Ali N, Saeed M (2020) Nanomaterials 10:849
19. Suryanarayana C, Inoue A (2013) Int Mater Rev 58:131–166
20. Chen N, Martin L, Luzguine-Luzgin DV, Inoue A (2010) Mater 3: 5320–5339
21. Lee P, Liu W, Lin C, Huang (2007) J Mater Sci Eng A 449:1095–1098
22. Yao D, Deng L, Zhang M, Wang X, Tang N, Li J (2015) Sci Rep 5: 8083
23. Sriharitha R, Murty B, Kottada RS (2014) J Alloy Comp 583:419–426
24. Takeuchi A, Inoue A (2005) Mater Trans 46:2817–2829
25. Turnbull D (1969) Contemp Phys 10:473–488
26. Wang Z, Wang R, Wang W (2006) Mater Lett 60:831–833
27. Qin C, Zhang W, Asami K, Kimura H, Wang X, Inoue A (2006) Acta Mater 54:3713–3719
28. Guo S, Liu Z, Chan K et al (2012) Mater Lett 84:81–84
29. An W, Cai A, Xiong X et al (2013) J Alloy Comp 563:55–62